Effects of Curvature in High Speed Inlets

Akshay S. Deshpande* and Jonathan Poggie†

Purdue University, West Lafayette, IN 47907-2045, USA

The sharp fin / flat plate geometry, which is representative of supersonic engine inlets, generates a complex three-dimensional interaction, stagnation pressure losses, and high heat loads. Alternatively, a curved fin can generate an isentropic compression, and consequently a higher pressure recovery and a lower level of heating. The three-dimensional flowfield generated by a 20 deg curved fin was investigated numerically via the Reynolds-Averaged Navier-Stokes equations, using the open-source computational fluid dynamics code SU2. The curved fin was placed in a Mach 3 flow with a freestream unit Reynolds number of 67×10^6 m^{-1}. The mean properties from the computational results were compared with the experimental data of Konrad et al. The results from computations agreed well with the experimental results and reproduced essential features of the flowfield. Model plasma actuators were implemented for the curved-fin case, and their effects on the crossflow, streamwise pressure gradient, and skin-friction coefficient were investigated. It was observed that application of actuators increased the three-dimensionality of the flowfield by amplifying the secondary flow in the boundary layer.

Nomenclature

$\vec{B}$	Magnetic field (T)	α	Angle of attack (deg)
C_f	Skin-friction coefficient	β	Azimuthal angle (deg)
C_H	Stanton number	δ	Boundary layer thickness (m)
E	Total energy (J/kg)	γ	Yaw angle (deg)
$\vec{F}$	Body force (N)	θ	Momentum thickness (m)
$\vec{I}$	Current vector (A)	μ	Dynamic viscosity (N-s/m^2)
$\bar{\bar{I}}$	Identity matrix	ρ	Density (kg/m^3)
K	Scaling factor (m^3)	$\bar{\bar{\tau}}$	Shear stress tensor (N/m^2)
L	Length of fin (m)		
M	Mach number	*Subscripts*	
p	Static pressure (Pa)	c	Center
Q	Power input (W)	e	Edge
q	Source term (N/m^3 or W/m^3)	i, j	Tensor indices
Re	Reynolds number	t	Total
S	Source term distribution (m^{-3})	w	Wall
T	Static temperature (K)	∞	Freestream
t	Time (s)		
U	Velocity component (m/s)	*Superscripts*	
V	Electric potential (V)	$+$	Inner units
W	Velocity component (m/s)		
$\vec{v}$	Velocity vector (m/s)		
w	Source term length scale (m)		
x	Streamwise coordinate (m)		
y	Wall-normal coordinate (m)		
z	Spanwise coordinate (m)		

---

*Graduate Research Assistant, School of Aeronautics and Astronautics, 701 W. Stadium Avenue. AIAA Student Member.
†Associate Professor, School of Aeronautics and Astronautics, 701 W. Stadium Avenue. AIAA Associate Fellow.

I. Introduction

Shock-wave / boundary-layer interaction continues to be one of the major challenges faced by inlet designers. Its adverse effects, such as low-frequency unsteadiness, flow distortion, drag, and heat transfer, compound the difficulty involved in attaining design flow conditions, and make the inlet susceptible to unstart. Most of the high-speed inlets used in practical application consist of a sharp-fin / flat-plate geometry, which has been studied extensively in the past, both experimentally [1–4] and numerically [5, 6].

The three-dimensional flowfield of a sharp-fin is shown in Fig. 1. The separated flowfield associated with a sharp fin develops conically downstream, with a vortex enclosed by the λ-shock foot. Smaller regions of secondary flow develop, depending on the freestream Mach number M_∞ and angle of attack α. Away from the walls, the shock is inclined with the freestream flow at the inviscid wave angle governed by the oblique shock relations. The sharp pressure rise generated by the oblique shock is responsible for the large-scale separation observed in Fig. 1. One way to avoid such separation would be to compress the flow to the same downstream pressure by continuous flow turning rather than an abrupt change of direction. Such an interaction can be obtained with a curved fin, as shown in Fig. 2.

This flow is characterized by a three-dimensional boundary layer with secondary crossflow, the magnitude of which increases with downstream distance. The flow faces an adverse pressure gradient in both the streamwise and spanwise directions. Unlike sharp-fin interactions, the curved-fin interaction does not separate. Previous experimental and computational studies of the flowfield structure were carried out by Konrad et al. [7–10]. The computational study employed the Baldwin-Lomax model, and the mean properties were validated with the experimental data. The present work aims to reproduce the mean flow results of Konrad et al., compare with qualitative results from the sharp-fin interaction observed in authors' previous work [4], and evaluate the potential effectiveness of plasma actuators for controlling this flow.

A typical plasma actuator consists of two electrodes flush-mounted on a dielectric surface. On applying a potential difference across the electrodes, a current is generated which forms an electrical discharge between them. If this assembly is placed in an external magnetic field perpendicular to the surface and current path, a magnetic body force is generated. This force provides additional momentum to the boundary layer to withstand the adverse pressure gradient imposed by a shock wave. It also alters the force balance with the wall shear stress, potentially reducing the extent of a separated zone [4]. Plasma actuators have promising aerospace applications owing to the absence of moving parts, a low profile when deactivated, and rapid response times to match short characteristic flow time scales [11].

In the authors' previous work [4], the effects of plasma actuators were investigated in a sharp-fin interaction. With the application of a single actuator, it was observed that characteristics of the interaction did not change significantly. Although heating from the actuator dominated the effect on the flow, application of bodyforce tended to produce an opposing effect. A case with multiple actuators was also proposed, and is tested in this study with an objective to reduce the secondary crossflow in the flowfield.
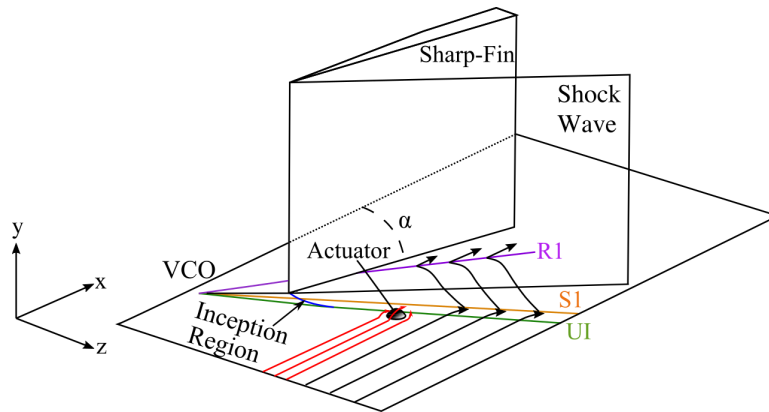

Fig. 1   Sharp-fin interaction [4].

II. Methodology

The solutions for the curved-fin case were obtained by Reynolds-Averaged Navier-Stokes (RANS) calculations using the SU2 code [12]. SU2 is an open-source, unstructured, finite-volume solver. For the present work, the compressible
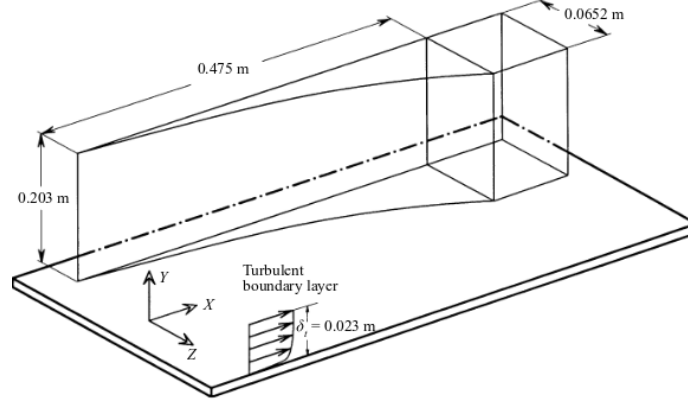
Fig. 2 Curved-fin domain. Reproduced from Ref. [9] under Cambridge University Press permission for use of a single figure.

Reynolds-averaged Navier-Stokes equations were solved in the following form:

$$\frac{\partial \rho}{\partial t} + \nabla \cdot (\rho \vec{v}) = 0 \tag{1}$$

$$\frac{\partial}{\partial t} (\rho \vec{v}) + \nabla \cdot \left(\rho \vec{v} \vec{v} + p \bar{\bar{I}} - \bar{\bar{\tau}} \right) = \vec{q}_M \tag{2}$$

$$\frac{\partial}{\partial t} (\rho E) + \nabla \cdot \left(\rho E \vec{v} + p \vec{v} - \bar{\bar{\tau}} \cdot \vec{v} - \vec{q} \right) = q_E \tag{3}$$

Here $\vec{q}_M$ and q_E are the source terms in a magnetohydrodynamic model of the plasma actuator.

The governing equations were closed with the one-equation Spalart-Allmaras turbulence model [13]. The inviscid fluxes were discretized using the AUSM scheme with MUSCL reconstruction at cell faces for second-order accuracy. The Venkatakrishnan slope limiter was used to preserve monotonicity of the solution near sharp gradients. The gradients of flow properties required for the computation of viscous fluxes were calculated using the Green-Gauss theorem. Solutions were marched to steady state using the implicit Euler scheme. The CFL number was maintained at 1.0 for the baseline cases and 0.5 for the cases in which the source term was switched on. The flow conditions (shown in Table 1) used in this computations were based on Konrad's experiments [7].

Table 1   Flow conditions.

Parameter	Value
u_∞	576 m/s
ρ_∞	0.794 kg/m^3
T_∞	100 K
$\rho_\infty u_\infty / \mu_\infty$	67×10^6 m^{-1}
M_∞	2.87
δ	25 mm
θ	1.02 mm
Re_θ	68000
$Re_{\theta i}$	27000

In Table 1), δ, θ, Re_θ are respectively the displacement thickness, momentum thickness, and momentum-thickness Reynolds number at the streamwise station aligned with the fin leading edge. The coordinates of the curved fin geometry were taken from Konrad's disseration [7]. The domain was 475 mm long, 203 mm high, and 152.4 mm wide. In accordance with the notation used by the experimentalists, the origin was located 76.2 mm upstream of the fin leading

3

edge. A turbulent boundary layer profile corresponding to the properties in Table 1 was imposed at the inlet. A streamwise region of approximately 10% of the fin length was constructed upstream of the fin leading edge to allow the imposed boundary layer profile to adjust numerically. A supersonic outflow boundary condition was set at the top boundary (y = 203 mm), spanwise boundary (z = 76.2 mm), and the outlet (x = 475 mm). A slip-wall boundary condition was imposed on the sidewall upstream of the fin ($x < 76.2$ mm, $z = -76.2$ mm). A no-slip adiabatic wall condition was applied on the fin surface and on the flat plate. The medium-resolution grid for the curved-fin geometry is shown in Fig. 3(a).

| (a) Curved-fin | (b) Curved-fin (flow-control) |
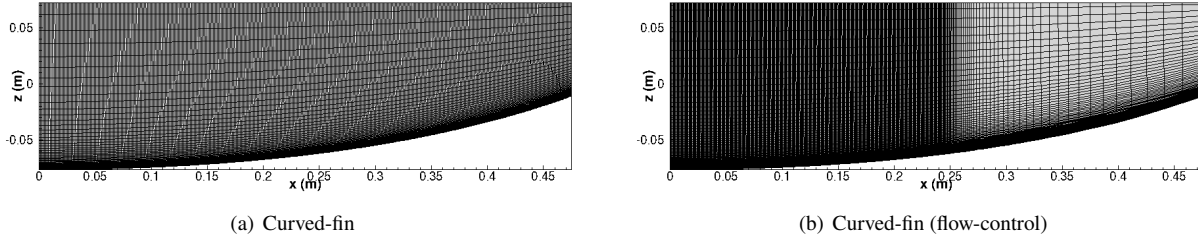
Fig. 3   Medium grids (top view).

A grid convergence study was carried out for the baseline calculations of the curved fin. The coarse grid consisted of $105 \times 50 \times 25$ cells, with $\Delta y^+ < 1$ at the wall. The medium and fine grids were constructed from the coarse grid by sequentially applying a grid refinement ratio of two, maintaining the grid spacing at the wall. The medium and fine grids thus consisted of $210 \times 100 \times 50$ cells and $420 \times 200 \times 100$ cells respectively. Clustering of cells was done in the wall-normal direction and spanwise direction, away from the fin surface.

For these preliminary calculations, Δy^+ on the fin was maintained at five. We acknowledge that this is not sufficient to resolve the flow at the corner of the fin and flat plate, which may have significant influence on the flow structure of the curved fin interaction. Calculations that better resolve this region of the flow are in progress.

Konrad [7] used three different coordinate systems to plot the results. The first was a Cartesian coordinate system with the origin shifted from the fin leading edge by 76.2 mm in the upstream direction and 76.2 mm in the spanwise direction (see Fig. 3). The second coordinate system was aligned with the streamlines of the outer inviscid flow, whereas the third was aligned with the mean flow direction at a specific wall-normal station. The different coordinate systems are shown in Fig. 4. Unless stated otherwise, the results in this paper are presented in the Cartesian (tunnel) coordinate systems on the center-plane (z = 0 m). For other plots, an appropriate coordinate transformation was used for comparison to the experimental data.
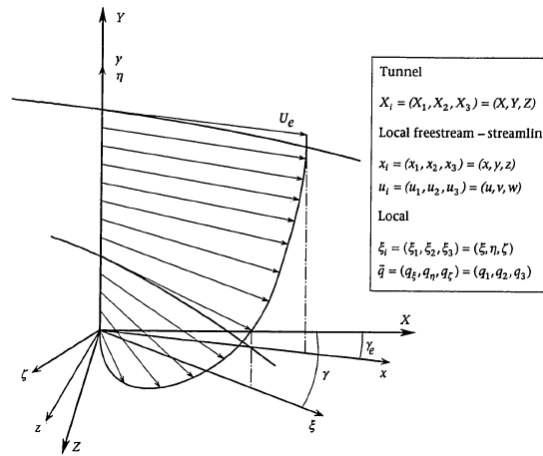

Fig. 4   Coordinate systems [7].

The plasma actuator considered here was based on the gliding surface discharge actuator studied experimentally by

Kalra et al. [14]. The plasma actuator was modeled with a semi-empirical magnetohydrodynamic formulation, as a dissipative Joule heat source and a magnetic body force, both with a Gaussian distribution in space. The formulation was based upon previous computational studies of such actuators [11, 15, 16]. It was assumed here that the energy input to the actuator goes entirely into the flow; losses to vibrational excitation or radiative heat transfer were neglected. Taking the coordinate axes as in Fig. 2, the mathematical expression for the source term is:

$$
\begin{aligned}
S(x, y, z) &= \frac{1}{K} \exp\left[-\left(\frac{x - x_c}{w}\right)^2 - \left(\frac{y - y_c}{w}\right)^2 - \left(\frac{z - z_c}{w}\right)^2\right] \\
\vec{q}_M &= \vec{F}\, S(x, y, z) \\
q_E &= \left(Q + \vec{F}\cdot\vec{v}\right) S(x, y, z)
\end{aligned}
\tag{4}
$$

Here the total magnetohydrodynamic body-force is $\vec{F} = (\vec{I} \times \vec{B})w$. The current and magnetic field were assumed to be perpendicular. The body force was directed upstream. The wall normal and spanwise components were set to zero. The total Joule heating is $Q = VI$, K is a scaling factor, (x_c, y_c, z_c) are the coordinates of the centroid of the actuator, and w is a characteristic length scale. The source term is scaled such that the integral, over all space, of the spatial distribution term $S(x, y, z)$ is unity. This condition requires that $K = \pi^{3/2}w^3$. For the case with application of plasma actuators, the medium grid for the baseline case was used, but it was refined near the source term locations (see Fig. 3(b)).

III. Results

The objective of the present project was to evaluate the potential effectives of plasma actuators in modifying the supersonic flowfield around a curved fin. Reynolds-averaged Navier-Stokes computations were carried out for two cases: the baseline flowfield corresponding to the experiments of Konrad et al. [7–10], and a flow control case with four plasma actuators based on the experiments of Kalra et al. [14].

A. Baseline Flow

First, the results of the baseline flow computations were compared to the experimental data. A grid convergence study was carried out using three grids. The coarse, medium, and fine grids consisted respectively of 1.31×10^5, 1.05×10^6, and 8.4×10^6 points. Fig. 5 shows the variation of the mean wall pressure and skin friction along the line $y = 0$ m, $z = 0$ m for the three grids.

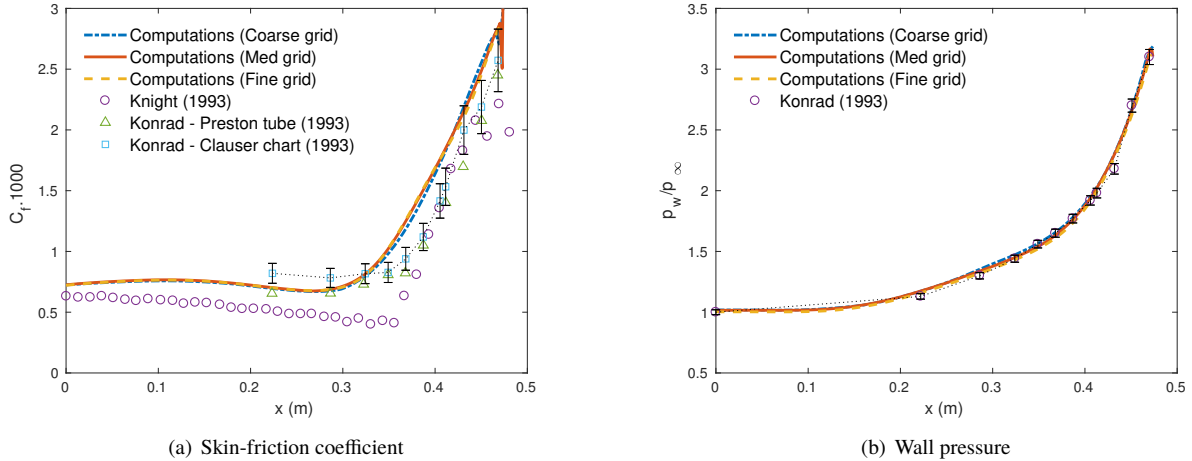(a) Skin-friction coefficient

(b) Wall pressure

Fig. 5   Grid convergence study.

The mean skin friction (Fig. 5(a)) and wall pressure (Fig. 5(b)) obtained from the present computations converge with increasing grid resolution. The skin-friction coefficient does not vary until the convergence line but rises rapidly downstream due to entrainment of inviscid high-momentum fluid into the boundary layer [8]. Unlike the skin-friction coefficient, the wall pressure begins to rise downstream of the upstream influence line.

5

Konrad [7] obtained the skin-friction coefficient experimentally using two approaches: the Clauser chart method and the Preston tube method. Results obtained with these two data reduction methods have been found to agree within ±10% in three-dimensional flows as long as the mean velocity profile contains a distinct logarithmic region. In the experiments of Konrad [7], a constant difference of 10–20% between the two methods was reported, and an experimental error of ±10% was estimated.

For an experimental uncertainty of ±10% in the mean skin friction, the comparison in Fig. 5(a) shows that the present computational results lie slightly outside the bounds of experimental uncertainty. The results from current study show a better agreement with the experimental data than the computations of Knight et al. [8], a result that might be attributed to the choice of turbulence model.

The wall pressure plot in Fig. 5(b) shows excellent agreement with the experimental data and lies within the experimental uncertainty of ±5% reported for static pressure measurements. The results shown henceforth are from the fine grid case.

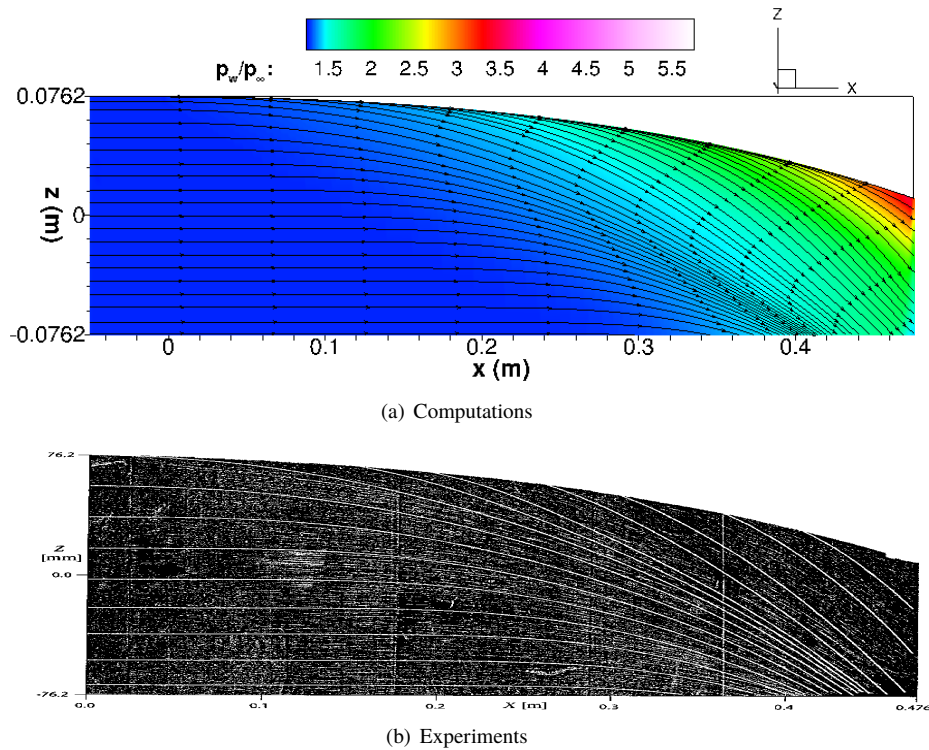

(a) Computations

(b) Experiments

Fig. 6   Limiting streamlines [7].

A plot of the limiting streamlines on the flat plate with color contours of mean wall pressure is compared with the surface flow visualization from Konrad's experiments in Fig. 6. Note that the coordinate system in Fig. 6(a) is switched to left-handed for the purpose of comparison with experiments. Streamlines from the computations show a close agreement with the experiments. A convergence line in the vicinity of $x = 0.4$ m, at the edge of the domain ($z = -76.2$ mm) can be observed.

The profiles of mean streamwise velocity are plotted at several locations both upstream and downstream of the convergence line in Fig. 7. The streamwise velocity is non-dimensionalized by the local edge velocity. The location of the mean convergence line ($x = 0.387$ m, $z = 0$ m) was taken from the experiments, and is used as a reference in all the computational results for ease of comparison. Before the mean convergence line, the flow is decelerated progressively due to the adverse pressure gradient generated by the compression waves. The profiles start to display an inflection point downstream of $x = 0.349$ m. The inflection point at the experimental location of the mean convergence line is prominent, thereby indicative of incipient separation. This behavior consistent with the primary separation line observed in the three-dimensional interaction of a sharp-fin geometry [4].

Downstream of the convergence line, the inflection point in the profiles starts to disappear and the profiles start to become fuller. The acceleration of flow downstream in the presence of an adverse pressure gradient is caused by
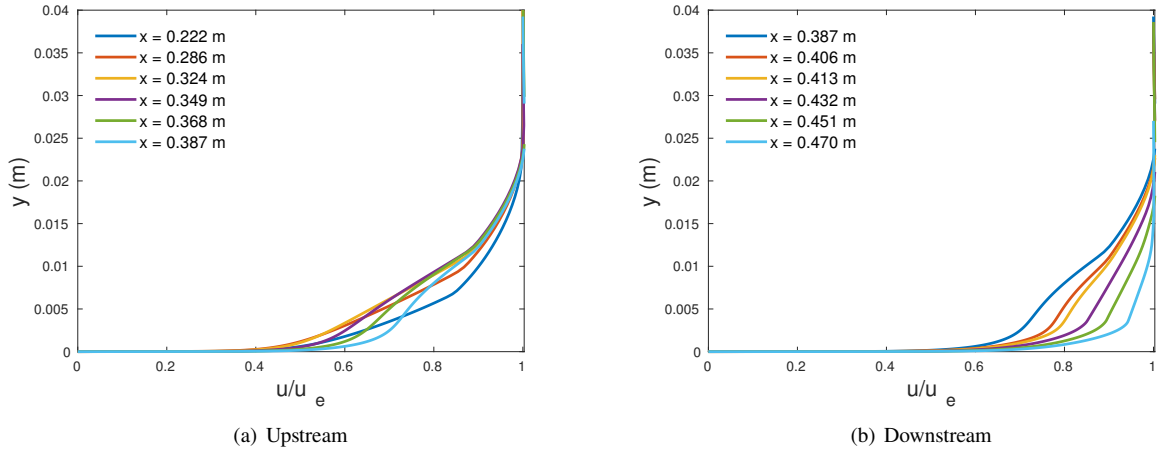
(a) Upstream

(b) Downstream

Fig. 7   Streamwise velocity profiles.

mixing high-momentum fluid from the incoming boundary layer with the low-momentum fluid near the wall [9]. This transportation of fluid can be attributed to the progressively increasing pressure gradients at the wall. Furthermore, from Figs. 7(a) and 7(b), it can be observed that the boundary layer thickness does not vary significantly.
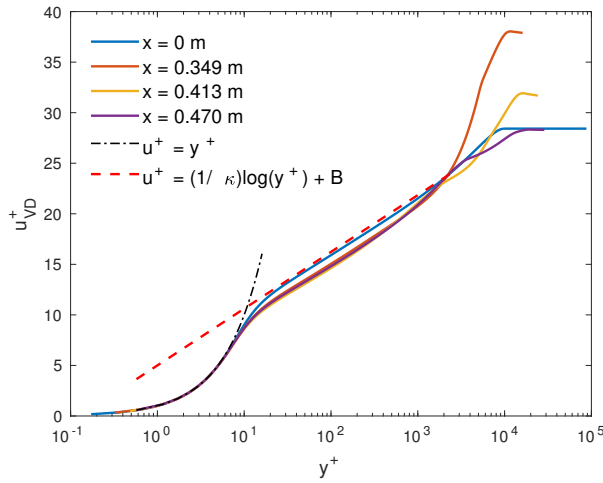

Fig. 8   Van-Driest transformed profiles.

The Van-Driest transformed velocity profiles in wall coordinates are shown in Fig. 8. The transformed velocity profile imposed at the inlet ($x = 0$ m) collapses nicely on the logarithmic law of the wall. Further downstream, the adverse pressure gradient causes the profile to deviate from the logarithmic overlap region due to thinning of the viscous sublayer, with an increasing wake component. Near the end of the domain ($x = 0.47$ m), the boundary layer starts to relax towards an equilibrium turbulent boundary layer profile, as evident from the smaller wake region.

The variation of yaw angles with respect to the wall normal direction, at different streamwise locations, is shown in Fig. 9. Overall, the computational results lie within the experimental uncertainty ($\pm 2°$) and agree well with the computational results of Knight [8]. For clarity, the error bars are plotted for every third point of the experimental data. The yaw angle at the wall (γ_w) was calculated by taking the arctangent of the ratio of shear stresses in the spanwise and streamwise directions, respectively. From the first point off the wall, yaw angle was computed from the arctangent of the ratio of the spanwise (w) and streamwise (u) velocity components. The differences in the computational and experimental results increase near the wall, which can be attributed to high uncertainty in the measured yaw angles for this region and to the limited validity of the turbulence model for highly three-dimensional flow.
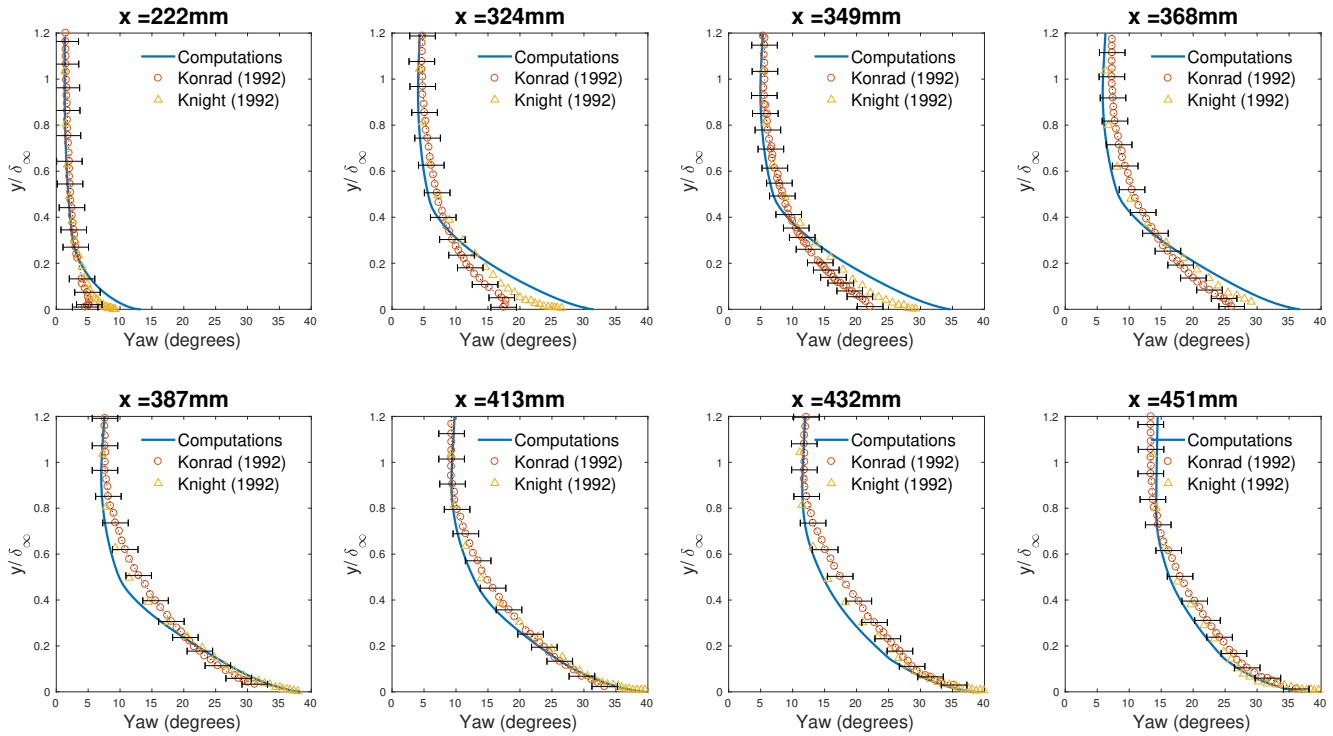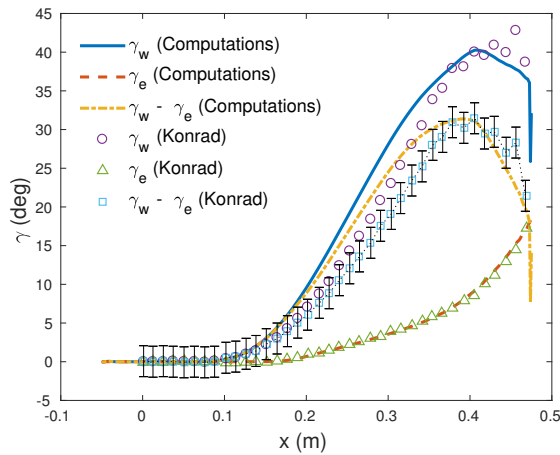
7

Fig. 9   Wall-normal profiles of yaw angle.

Fig. 10   Streamwise profiles of yaw angle.

Figure 10 compares the streamwise variation of the wall flow angle (γ_w), free-stream flow angle (γ_e) and the deviation in flow direction across the boundary layer ($\gamma_w - \gamma_e$) with the experimental values. The predicted freestream yaw angle shows excellent agreement with the experimental values, which is expected for the inviscid flow in that region. For yaw angles at the wall, the disagreement between experimental and computational results increases downstream.

Johnston [17] proposed a triangular model for polar plots of velocity from three-dimensional boundary layers with secondary flow. The coordinate system used to derive the model was aligned with the main flow streamlines (freestream streamline coordinates). The model splits the boundary layer in two regions: the inner region adjacent to the wall, and
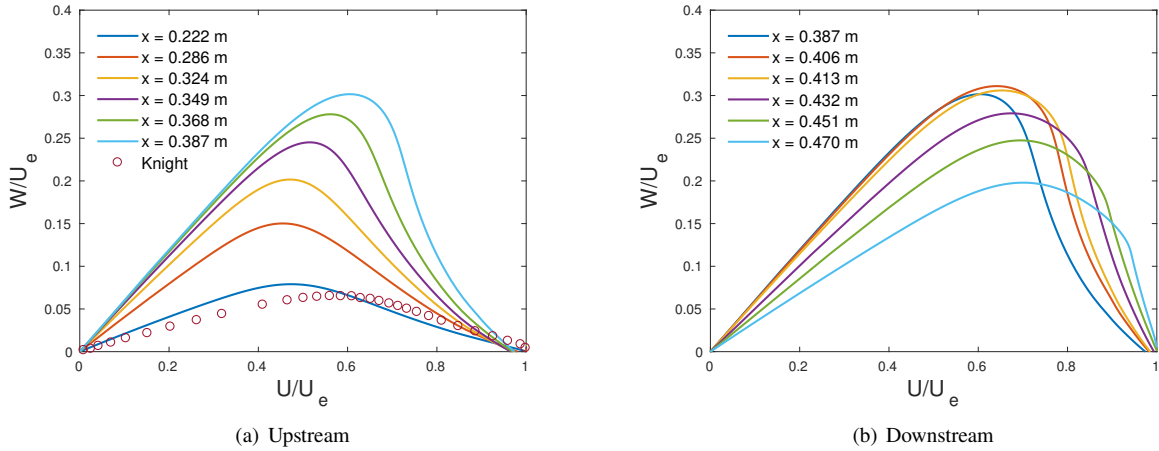
(a) Upstream

(b) Downstream

Fig. 11   Polar plots (in freestream-streamline coordinates).

the outer region adjacent to the main flow. In region I, the velocities follow a simple, linear relation: $W/U_e = eU/U_e$ where $e = \tan \gamma_w$. In region II, the velocities are expressed by the relation: $W/U_e = A(1 - U/U_e)$. In these relations, U, W are the velocity components in a horizontal plane and U_e is the edge velocity, with the coordinate system aligned with the inviscid streamline (see Fig. 4). The parameter A depends on the flow turning angle (α) as follows:

$$A = -2U_e^2 \int_0^\alpha \frac{d\alpha}{U_e^2} \qquad (5)$$

For a relatively simple flows, U_e is constant along the streamline. In such cases, the equation in Eq. (5) reduces to $A = -2\alpha$.

This model was derived from the experiments carried out by Johnston, which were incompressible in nature [17]. A perturbation analysis carried out by Konrad [7], was restricted to the outer part of the boundary layer (for assumption of small velocity gradients) and regions small crossflow (for assumption of small velocity defects). It suggested that the triangular model is valid for compressible boundary layer, in terms of Favre-averaged velocities.

Figure 11 shows the polar plots of velocities at different stations. The polar plots in Fig. 11 resemble the Johnston triangular profile for stations that are farther upstream. The polar profile at $x = 0.222$ m shows satisfactory agreement with the computational profile predicted in Knight's calculations. The mismatch of slope in region I $(e = \tan \gamma_w)$ between current computations and Knight's calculations can be attributed to the different turbulence models used. This difference in the initial slope causes the peaks to be slightly misaligned, but the slopes in region II agree well. From the polar plots, it can be observed that the crossflow component increases rapidly downstream and the plots lose their characteristic triangular shape. Given the assumptions in Johnston's analysis, the triangular model can be expected to be invalid at these locations. The peak of the plot moves towards the higher U-velocity values, which correspond to a higher wall-normal coordinate. Downstream of the mean convergence line, the crossflow component starts to drop as the boundary layer relaxes to an equilibrium state.

Figure 12 plots the variation of Pitot pressure ratio along the wall-normal direction. For locations upstream of the mean convergence line, the computational results agree well with both the experiments and Knight's calculations in the outer part of the boundary layer. The experimental uncertainty in Pitot pressure measurement is $\pm 2\%$ [7]. The trend of under-prediction of near wall gradients in Knight's computations is reproduced in this study. Downstream of the convergence line, the computations seem to capture the near-wall gradients with reasonable accuracy, but display increasing differences downstream and away from the wall, where the Pitot pressure gradients are highest.

Starting from the left $(p_s/p_\infty = 1)$, Fig. 13 plots static pressures at locations $x = 0.222$ m, 0.324 m, 0.349 m, 0.387 m, 0.432 m, and 0.451 m, respectively. As expected, the static pressure does not vary significantly across the boundary layer for high Reynolds number flows. The computational results lie well within the experimental uncertainty band of $\pm 5\%$ and show better agreement with experimental data than Knight's computational results. The errorbars are plotted for every fifth experimental data point for clarity.

Figure 14 shows the three-dimensional mean flowfield. The stream ribbons are colored by the U-velocity contours.
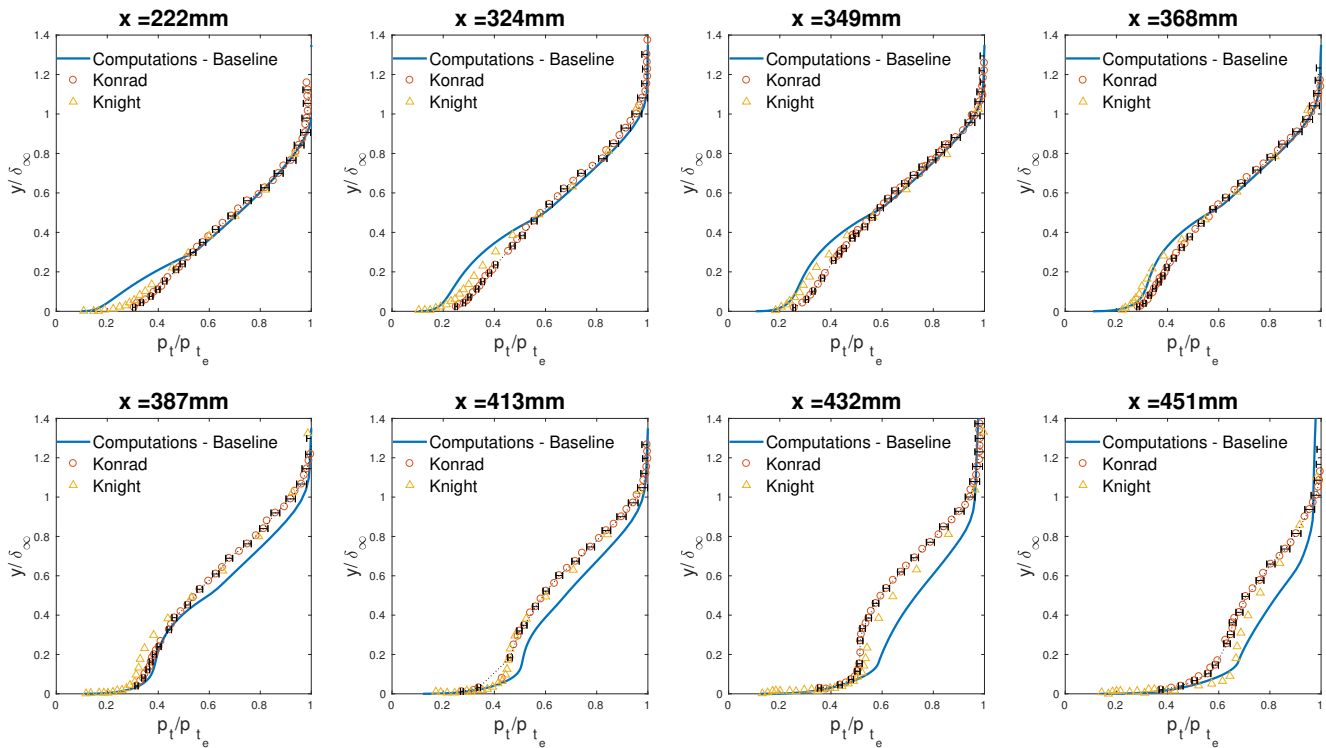
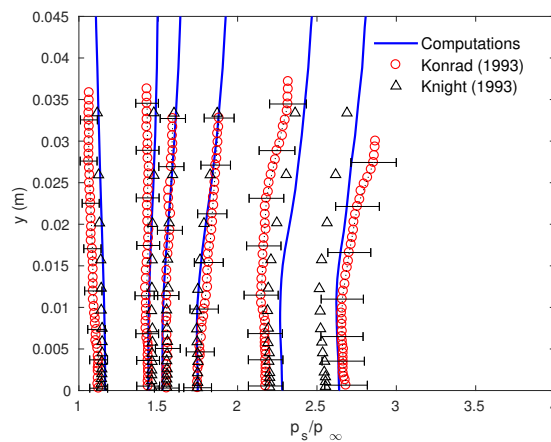**Fig. 12   Pitot pressure ratios (at constant *x*).**

Fig. 13   Static pressures.

Limiting streamlines and wall pressure contours are also included in the $y = 0$ m plane. Acceleration of flow close to the wall, in-spite of an adverse pressure gradient, can be observed clearly. The transport of high-momentum fluid from the freestream towards the wall can be inferred from the streamlines stacked vertically, close to the fin surface. The crossflow component is first generated near the fin surface, farther upstream where the flow initially begins to turn. The low momentum fluid close to the wall is deflected by a larger magnitude than the flow away from the wall. This differential turning is also observed in the sharp-fin interaction, which generates a helical vortex post separation [4]. In this case, as the flow is resistant to the adverse pressure gradient, it does not roll up to form a separation vortex.

Subject to these observations, Konrad and Smits [9] divided the flowfield into three distinct regions: the small
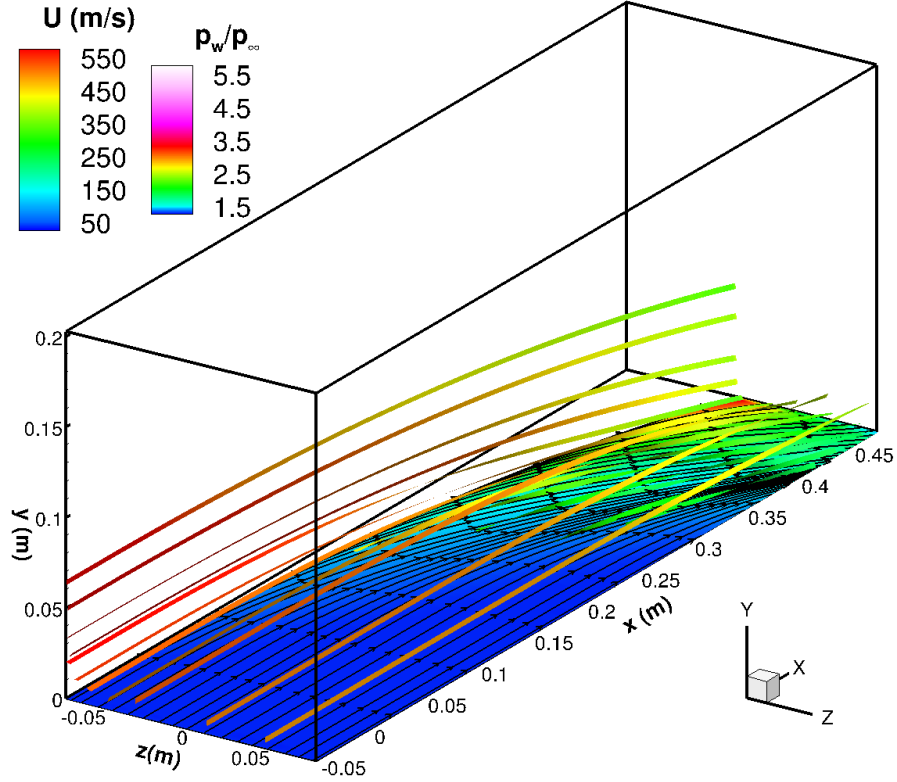
Fig. 14   Three-dimensional flowfield.

crossflow region, the upstream convergence region, and the downstream convergence region. Based on the the Johnston triangular plots, the threshold small crossflow angle was determined to be 10°. In this region, apart from the validity of the triangular model, the flow is weakly three-dimensional and the law of the wall holds. The upstream convergence region is characterized by increased cross flow ($\approx 20°$) and inflection point in the velocity profiles (see Fig. 7) on account of adverse pressure gradient. The downstream convergence region experiences strong three-dimensional effects. The mixing of high-momentum fluid from upstream flow with low-momentum fluid in the near the wall occurs in this region which results in a fuller boundary layer profile (see Fig. 7(b)). This phenomena also leads to steeper Pitot pressure gradients in the outer part of the boundary layer (see Fig. 12). The turbulent boundary layer profile follows the law of the wall in the viscous sublayer (where $u^+ = y^+$), but does not collapse on the logarithmic region. According to Konrad and Smits, the primary effect of streamline curvature was generation of a lateral pressure gradient, in addition to a longitudinal adverse pressure gradient. On comparing with an experimental case in which the flow was essentially two-dimensional and subjected to a similar longitudinal pressure gradient, the skin-friction for Konrad's case was 20% higher owing to displacement of high-momentum fluid towards the wall.

B. Flow control

Next, the effects of applying plasma actuators in the three-dimensional flowield were explored. The actuator parameters were adapted from Deshpande and Poggie [4]. A current value was set to $I = 100$ mA with an applied potential difference $V = 5$ kV. These values fall in the range of current and voltage values used by Kalra et al. in their experiments [14]. The power input to the actuator was $Q = IV = 500$ W and the corresponding non-dimensional power was $Q/(\rho_\infty u_\infty^3 \delta_\circ^2) = 5.28 \times 10^{-3}$, where $\delta_\circ$ is the boundary layer thickness at the fin leading edge. This value indicates that the power in the freestream flow is dominant over the power input to the actuator. To overcome this issue, four actuators were placed roughly along the upstream influence line, which meant a gross power of 2 kW (500 W each) was provided by the external circuit. The coordinates of centers of the actuators are given in Table 2.

For comparison with the baseline case, one of the four actuators was placed on the center-plane. The width of the source term was maintained at $w = 2$ mm, to place it well within the boundary layer in order to perturb the viscous

Table 2   Actuator locations.

Actuator	x_c (m)	y_c (m)	z_c (m)
1	0.047	0.0	-0.048
2	0.073	0.0	-0.033
3	0.099	0.0	-0.016
4	0.125	0.0	0.0

flow. The source term was assumed to have a spherical distribution, following Eq. (4). Since it is centered at the wall, a hemispherical disturbance is introduced in the flowfield. The actuators were placed in an external magnetic field, and the body force generated was oriented upstream. The magnetic field for this purpose was chosen to match the experiments [14], where its magnitude was 3.0 T. For a current of 100 mA, the total magnitude of the force generated was $4|\vec{F}| = 4IBw = 24 \times 10^{-4}$ N. The limiting streamlines on wall density contours in the presence of these actuators are shown in Fig. 15.
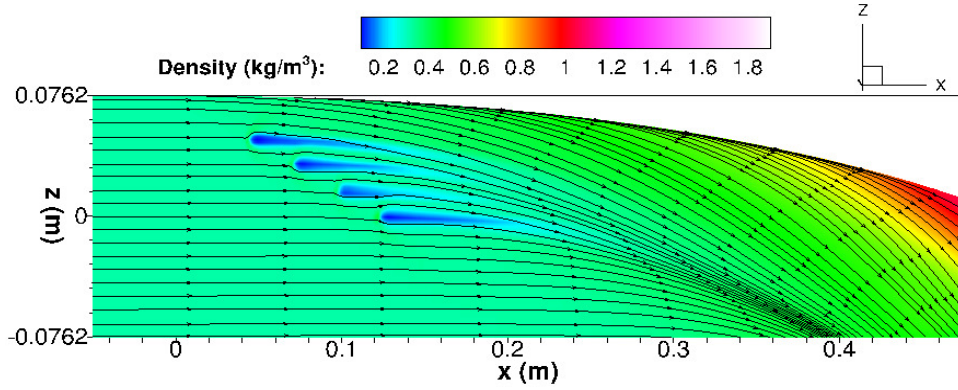
Fig. 15   Limiting streamlines.

In Fig. 15, low density regions coincide with the actuator stations. A distinct change in the flow footprint can be observed near the actuator locations, where the flow is deflected around them. On comparing Fig. 15 with Fig. 6(a), the location of convergence line at the edge of the domain ($z = 0.0762$ mm) seems to have moved slightly upstream for the case with actuators. The wake of the actuators conforms to the local flow direction near the wall. Apart from these changes, the overall flowfield is not affected significantly as the effect of actuators is localized to the near-wall region. The variation of wall properties in streamwise direction is compared with the baseline case in Fig. 16.

The actuator location labeled in Figs. 16(a) and 16(b) corresponds to 4th actuator in Table 2. The skin-friction coefficient in Fig. 16(a) decreases downstream of the actuator location before collapsing with on the baseline plot after the convergence line. Addition of heat increases the shape factor of the boundary layer, which decreases the velocity gradient $\partial u/\partial y$ at the wall. This results in a lower shear stress, and hence a lower skin-friction coefficient. The valley and peak in the skin-friction coefficient close to the actuator location is associated with the separation and reattachment of flow, immediately upstream and downstream of the actuator respectively. The brief separation of flow is caused due to an upstream orientation of the bodyforce. The skin-friction coefficient for the case with actuators begins to rise at a location upstream than that for the baseline case. This confirms an upstream movement of the mean convergence line.

The pressure plots in Fig. 16(b) remain mostly invariant with the application of flow control. The localized peak at the actuator location is caused by a weak bow shock at its leading edge. Since the total pressure rise remains same, it can be concluded that the total flow turning angle does not change. To check the effect of actuators on secondary flow, the yaw angle at the wall is shown in Fig. 17.

The yaw angle at the wall increases slightly upstream and downstream of the actuator. Farther downstream, it relaxes towards the baseline value. The yaw angle at the wall is calculated as $\tan^{-1}(\tau_{wz}/\tau_{wx})$. Based on this expression, an increase in yaw angle entails either a higher value of τ_{wz}, or a lower value of τ_{wx}. Based on the skin-friction coefficient plot in Fig. 16(a), a lower value of τ_{wx} seems to be more a likely cause.

(a) Skin-friction coefficient   (b) Wall pressure
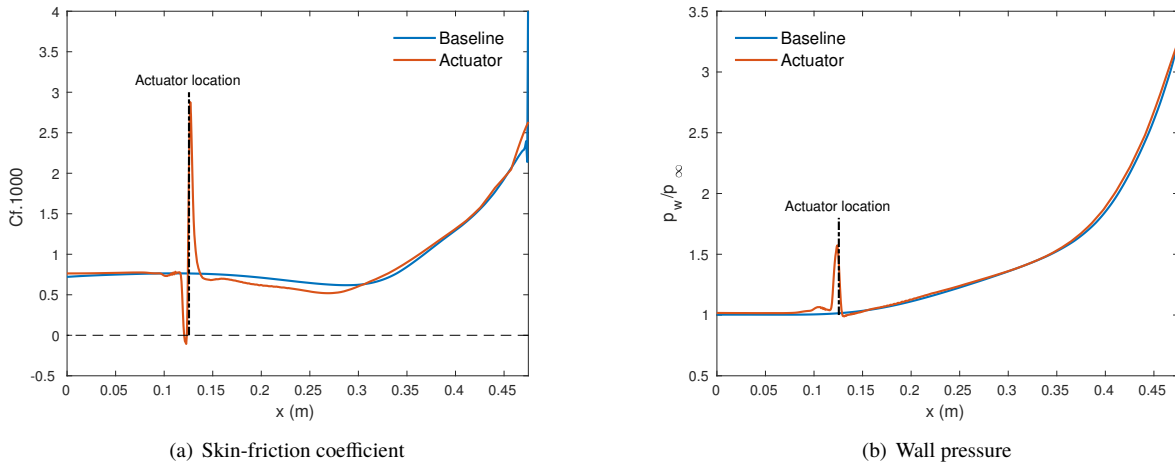
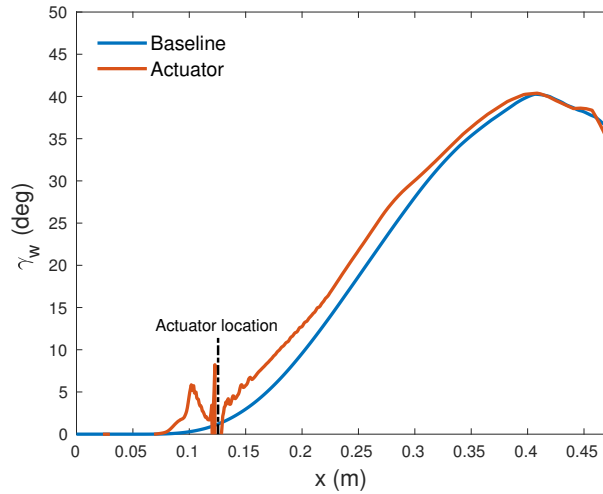**Fig. 16   Wall properties.**

Fig. 17   Yaw angle (at $y = 0$ m).

The polar plots in freestream-streamline coordinates are shown in Fig. 18. The dotted lines correspond to the baseline case, with the streamwise stations color coded according to Fig. 11. Upstream of the experimental convergence line, the application of actuators amplifies the crossflow component. The degree of amplification subsides downstream. The actuators have no notable effect on the polar plots downstream of the convergence line. These observations suggest that actuators influence the flow only a short distance downstream of their centers.

The wall-normal variation of yaw angles is plotted at streamwise stations close to the actuator in Fig. 19. The title of each subplot is the distance downstream from the actuator location, $(x_c, y_c, z_c) = (0.12555, 0.0, 0.0)$ m. The profiles is show considerable variation up-to $\Delta x \approx 10$ mm and collapse on the baseline profile after $\Delta x \approx 20$ mm. Another noticeable feature in the plots for flow control is the divergence from baseline plots observed close to the boundary layer edge. From Fig. 10, the freestream flow turning angle is less than $1°$ at the locations in Fig. 19. Therefore, deflection of flow by the leading edge shock associated with the actuator most likely causes this phenomenon. The yaw angle profile at $x = 0.13$ m decreases briefly close to wall before increasing again. But the overall trend suggests an increase in the crossflow with application of flow control.
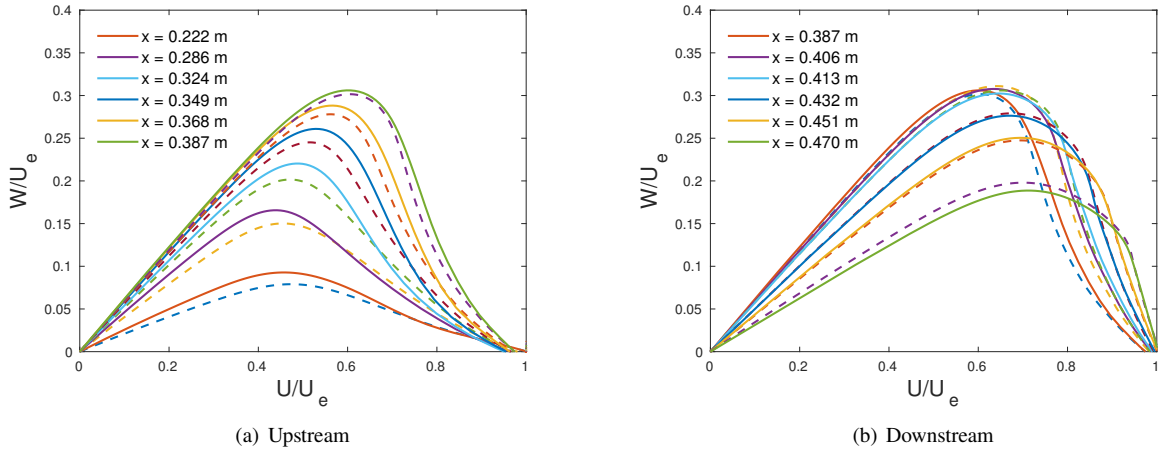
(a) Upstream

(b) Downstream

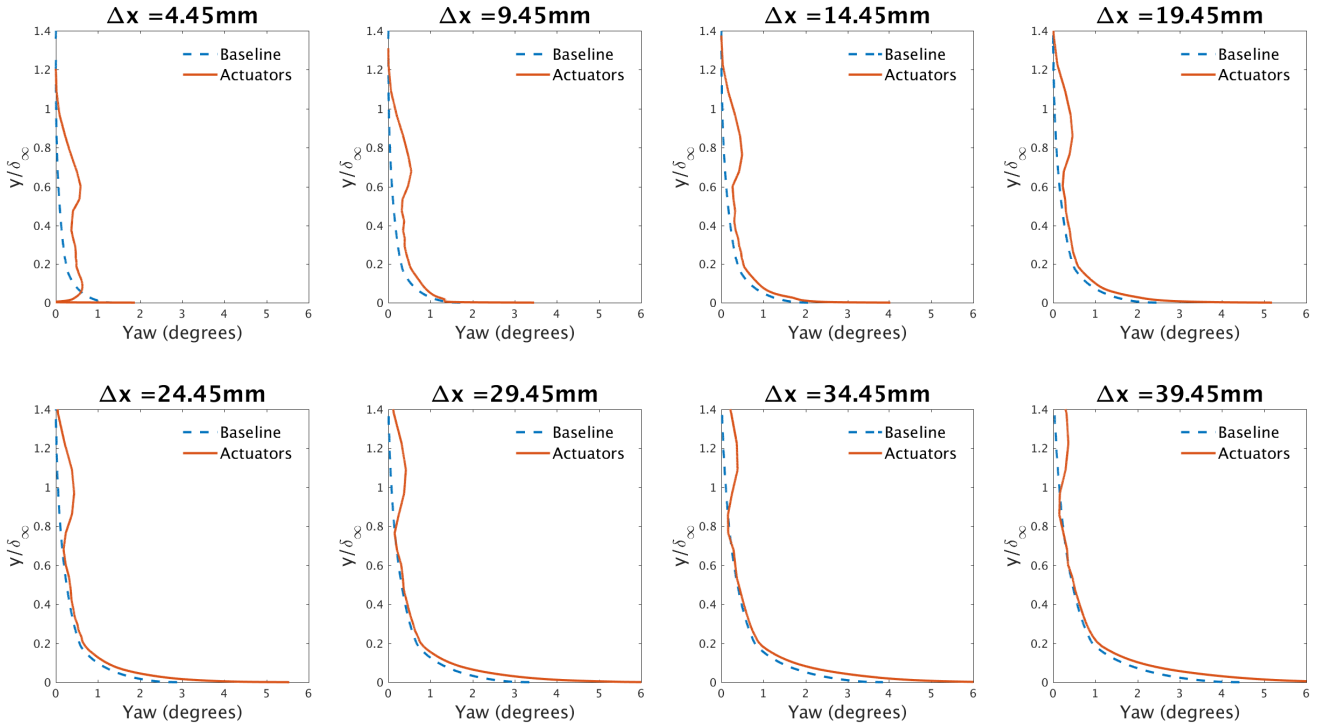**Fig. 18   Polar plots (in freestream-streamline coordinates).**

Fig. 19   Yaw angles (at constant *x*).

IV. Conclusions

Reynolds-Averaged Navier-Stokes calculations were carried out with the open-source computational fluid dynamics code SU2 to examine the mean flowfield associated with a curved-fin geometry. The flow parameters corresponded to the experiments carried out by Konrad [7]. A turbulent boundary layer profile corresponding to the conditions at the fin leading edge was imposed at the inlet. The computational results were compared with Konrad's experimental results as well as computations carried out by Knight using the algebraic one-equation Baldwin-Lomax turbulence model. Since the flow was attached throughout the domain, the Spalart-Allmaras turbulence model predicted the flow properties with

14

reasonable accuracy and captured essential features of the resulting three-dimensional flowfield.

The SU2 code was modified to include source terms in the momentum and energy equations as a semi-empirical model of a plasma actuator. The effects of the actuator on the three-dimensional flowfield were investigated. The application of flow control led to a slight upstream movement in the mean convergence line. The skin-friction coefficient decreased downstream of the actuator and approached the baseline value close to the domain exit. The total flow turning angle was unaffected. An increase in the yaw-angle at the wall caused by a lower streamwise shear stress was observed. The crossflow component in the boundary layer was amplified at locations upstream of the experimental mean convergence line and remained unchanged downstream. Application of plasma actuators led to an overall rise in yaw-angles at any given wall-normal location. Therefore, the configuration of actuators used in this study contributed towards the secondary flow, thereby increasing the extent of three-dimensionality of the flowfield.

It is worthwhile to investigate different configurations of actuators that reduce the secondary flow component in boundary layers. These configurations can then be used in applications such as improving inlet designs by reducing the extent of differential turning in order to prevent potential breakdown to a vortex like structure, and efficient wing design by damping the crossflow instability to cut down aerodynamic drag and increase fuel efficiency to name a few.

Acknowledgements

References

[1] Lu, F., "Fin generated shock-wave boundary-layer interactions," Ph.D. thesis, Department of Mechanical Engineering, The Pennsylvania State University, State College, PA, 1988.

[2] Garg, S., and Settles, G., "Unsteady pressure loads generated by swept-shock-wave/boundary-layer interactions," *AIAA Journal*, Vol. 34, No. 6, 1996, pp. 1174–1181.

[3] Settles, G. S., and Lu, F., "Conical similarity of shock/boundary-layer interactions generated by swept and unswept fins," *AIAA Journal*, Vol. 23, No. 7, 1985, pp. 1021–1027.

[4] Deshpande, A. S., and Poggie, J., "Flow Control of Swept Shock-Wave / Boundary-Layer Interaction using Plasma Actuators," *Journal of Spacecrafts and Rockets*, accepted for publication, 2018.

[5] Knight, D., Yan, H., Panaras, A. G., and Zheltovodov, A. A., "Advances in CFD prediction of shock wave turbulent boundary layer interactions," *Progress in Aerospace Sciences*, Vol. 39, No. 2, 2003, pp. 121–184.

[6] Leger, T., Bisek, N., and Poggie, J., "Computations of Turbulent Flow over a Sharp Fin at Mach 5," *Journal of Thermophysics and Heat Transfer*, Vol. 30, No. 2, 2016, pp. 394–402.

[7] Konrad, W., "A three-dimensional supersonic turbulent boundary layer generated by an isentropic compression," Ph.D. thesis, Princeton University, 1993.

[8] Konrad, W., Smits, A. J., and Knight, D., "A combined experimental and numerical study of a three-dimensional supersonic turbulent boundary layer," *Experimental Thermal and Fluid Science*, Vol. 9, No. 2, 1994, pp. 156–164.

[9] Konrad, W., and Smits, A. J., "Turbulence measurements in a three-dimensional boundary layer in supersonic flow," *Journal of Fluid Mechanics*, Vol. 372, 1998, pp. 1–23.

[10] Konrad, W., Smits, A. J., and Knight, D., "Mean Flowfield Scaling of Supersonic Shock-Free Three-Dimensional Turbulent Boundary Layer," *AIAA Journal*, Vol. 38, No. 11, 2000, pp. 2120–2126.

[11] Bisek, N., Rizzetta, D. P., and Poggie, J., "Plasma Control of a Turbulent Shock Boundary-Layer Interaction," *AIAA Journal*, Vol. 51, No. 8, 2013, pp. 1789–1804.

[12] Palacios, F., Colonno, M. R., Aranake, A. C., Campos, A., Copeland, S. R., Economon, T. D., Lonkar, A. K., Lukaczyk, T. W., Taylor, T. W., and Alonso, J. J., "Stanford University Unstructured (SU2): An open-source integrated computational environment for multi-physics simulation and design," *AIAA Journal*, Vol. 54, No. 3, 2016, pp. 828–846.

[13] Spalart, P., and Allmaras, S., "A One-Equation Turbulence Model for Aerodynamic Flows," AIAA Paper 1992-0439, American Institute of Aeronautics and Astronautics, Reston, VA, January 1992.

[14] Kalra, C. S., Zaidi, S. H., Miles, R. B., and Macheret, S. O., "Shock Wave / Turbulent Boundary Layer Interaction Control using Magnetically Driven Surface Discharges," *Physics of Fluids*, Vol. 21, 2009, 106101.

[15] Bisek, N., Boyd, I. D., and Poggie, J., "Numerical Study of Plasma-Assisted Aerodynamic Control for Hypersonic Vehicles," *Journal of Spacecraft and Rockets*, Vol. 46, No. 3, 2009, pp. 568–576.

[16] Atkinson, M. D., Poggie, J., and Camberos, J., "Control of Separated Flow in a Reflected Shock Interaction using a Magnetically-Accelerated Surface Discharge," *Physics of Fluids*, Vol. 24, 2012, 126101.

[17] Johnston, J. P., "On the three-dimensional turbulent boundary layer generated by secondary flow," *Journal of Basic Engineering*, Vol. 82, No. 1, 1960, pp. 233–246.